Two mechanisms of modulation of very-large-scale motions by inertial particles in open channel flow

G. Wang[1] and D. H. Richter[1],†

[1]Department of Civil and Environmental Engineering and Earth Sciences, University of Notre Dame, Notre Dame, IN 46556, USA

Very-large-scale motions (VLSMs) and large-scale motions (LSMs) coexist at moderate Reynolds numbers in a very long open channel flow. Direct numerical simulations two-way coupled with inertial particles are analysed using spectral information to investigate the modulation of VLSMs. In the wall-normal direction, particle distributions (mean/preferential concentration) exhibit two distinct behaviours in the inner flow and outer flow, corresponding to two highly anisotropic turbulent structures, LSMs and VLSMs. This results in particle inertia's non-monotonic effects on the VLSMs: low inertia (based on the inner scale) and high inertia (based on the outer scale) both strengthen the VLSMs, whereas moderate and very high inertia have little influence. Through conditional tests, low- and high-inertia particles enhance VLSMs following two distinct routes. Low-inertia particles promote VLSMs indirectly through the enhancement of the regeneration cycle (the self-sustaining mechanism of LSMs) in the inner region, whereas high-inertia particles enhance the VLSM directly through contribution to the Reynolds shear stress at similar temporal scales in the outer region. This understanding also provides more general insight into inner–outer interaction in high-Reynolds-number, wall-bounded flows.

Key words: particle/fluid flow, turbulence simulation

1. Introduction

Very-large-scale motions (VLSMs) extending to over $20h$ (where h is the boundary layer thickness) are found in very-high-Reynolds-number, wall-bounded turbulent flows and are distinct from the well-understood large-scale motions (LSMs) which form canonical streaks and hairpin vortices (Hutchins & Marusic 2007; Jiménez 2011; Smits, McKeon & Marusic 2011). These long, meandering features are observed to be energetic, carrying 40 %–65 % of the kinetic energy and 30–50 % of the Reynolds shear stress in pipe flow (Balakumar & Adrian 2007) or in turbulent boundary layers (Lee & Sung 2011), which is contradictory to the notion of 'inactive' motion proposed by Townsend (1980). In environmental flows, these anisotropic structures also have significant influence on the dispersion of pollutants, sand and other constituents.

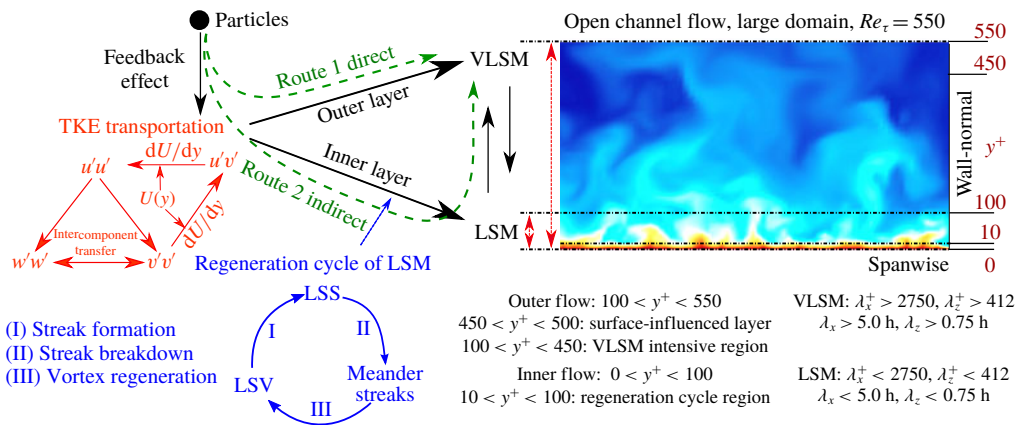† Email address for correspondence: David.Richter.26@nd.edu

FIGURE 1. (Colour online) Schematic of two routes of inertial particle effects on VLSMs through direct impact on turbulent kinetic energy transportation or via indirect upscale energy transfer from LSMs. On the right are streamwise velocity contours in the cross-stream plane of $Re_\tau = 550$ open channel flow (the flow simulated here) and the flow regions. The scale of definition of VLSMs and LSMs used in this study is based on del Álamo & Jiménez (2003). At the bottom left is an illustration of the regeneration cycle of near-wall turbulent structures proposed by Hamilton, Kim & Waleffe (1995).

At the same time, understanding the modulation of turbulence by inertial particles is itself a formidable challenge (Balachandar & Eaton 2010), and nearly all numerical studies of two-way coupling in particle-laden wall turbulence have been restricted to low Reynolds numbers. It is therefore the aim of this investigation to study the effects of particles on VLSMs, in particular focusing on the question of whether particles act directly or indirectly on these very large motions.

In contrast to VLSMs, the importance of LSMs on the flow dynamics in the near-wall region has been demonstrated in many different contexts. The LSMs are found to follow a self-sustaining process (i.e. a regeneration cycle) characterized by three key structures shown in the lower left of figure 1: large-scale streaks (LSSs), large-scale vortices (LSVs) and meandering streaks. Associated with these structures are three regeneration processes: streak formation, streak breakdown and vortex regeneration (Hamilton *et al.* 1995; Waleffe 1997; Schoppa & Hussain 2002). The particle modulation of the regeneration cycle has been investigated by Brandt (2014), Wang, Abbas & Climent (2018) and Wang & Richter (2019) to explain the non-monotonic effect of the onset of transition with mass loading and particle size. The typical scales of VLSMs, meanwhile, are far larger than LSMs, with their spanwise wavelength $\lambda_z \geqslant h$ and their streamwise wavelength $\lambda_x \geqslant 10h$ (Kim & Adrian 1999; Guala, Hommema & Adrian 2006; Adrian & Marusic 2012). These structures coexist with LSMs, and the interaction between them is still an open question. It is generally accepted that the regeneration cycle of LSMs does not require the existence of VLSMs (Jiménez & Pinelli 1999; Guala *et al.* 2006), and Hwang & Bengana (2016) propose that the formation of LSMs and VLSMs results from different mechanisms. Rawat *et al.* (2015) argue that VLSMs are self-sustained and do not draw energy from LSMs in the buffer layer; however, Kim & Adrian (1999) and Adrian & Marusic (2012) suggest that VLSMs are not a new type of turbulent structure but are merely the consequence of the alignment of coherent

LSMs. Toh & Itano (2005) show numerically that LSMs and VLSMs interact in a co-supporting cycle. Recent work by Lee & Moser (2019) reveals that very near the wall ($y^+ < 15$) there is a true inverse scale transfer from the dominant LSMs to VLSMs, which appears to be driven by interaction of the streaks with large-scale outer-layer structures. In the current work, we find that the enhancement of VLSMs can be caused by the promotion of LSMs via inertial particles.

A wide-ranging parameter space including flow type, mass fraction and particle-to-fluid length and time scale ratios can be expected to complicate the picture of turbulence modulation, resulting in poorly mapped out mechanisms of particle two-way coupling (Balachandar & Eaton 2010). In isotropic turbulence, Poelma & Ooms (2006) reviewed particle influences on the turbulent kinetic energy (TKE) spectrum of the carrier fluid, indicating that low wavenumbers are suppressed, while energy is gained at higher wavenumbers. The physical explanations are still not well understood, however. The situation is even more complex for wall-bounded turbulence, especially in the logarithmic layer, which contains a multiscale momentum cascade in three-dimensional space (Jiménez 2011, 2018; Marusic & Monty 2019), while the particle-to-fluid length and time scale ratios also vary as a function of wall-normal height. In addition, the wall-normal TKE transport is also modulated by inertial particles; for example, Zhao, Andersson & Gillissen (2013) found that inertial particles transported within streaky motions act as a carrier transferring TKE from the core region of the channel to the fluid close to the wall. There has been substantial progress in understanding inertial particle dynamics in the inner layer (i.e. related to LSMs); for instance, the phenomena of particle clustering and segregation (Pan & Banerjee 1995; Marchioli & Soldati 2002; Sardina *et al.* 2012), drag reduction (Dritselis & Vlachos 2008), high particle loading and cluster dynamics (Capecelatro, Desjardins & Fox 2018), particle inducing upscale energy transfer and transportation (Richter 2015), and regeneration cycle modulation (Wang & Richter 2019). However, to the best of our knowledge, very little attention has been paid to particle clustering and modulation of VLSMs in the outer layer.

More generally, it is inherently difficult to describe turbulence modulation by particles. The intensity of TKE is often used to indicate turbulence modulation (e.g. Pan & Banerjee 1996; Crowe 2000; Tanaka & Eaton 2008). However, this can lead to somewhat contradictory descriptions. For instance, recent observations have shown that, even though TKE is nearly unchanged, the onset of laminar-to-turbulent transition can be significantly advanced by particles with a low Stokes number ($St^+ = O(1)$; based on viscous time scale); see for example Saffman (1962), Michael (1964), Klinkenberg *et al.* (2013) and Wang & Richter (2019). In fact, not all scales of turbulence are enhanced during turbulence augmentation, so using the bulk TKE might misrepresent the modulation at certain length and time scales. This can be observed with spectral analysis, which is a natural means to study particle modulation of turbulence. For example Elghobashi & Truesdell (1993) found there is a possible so-called reverse cascade which tends to build up energy in large-scale structures in homogeneous turbulence, and Richter (2015) demonstrates that this upscale influence is a strong function of particle inertia. As a result, particles can influence turbulence scales far removed from their own response time scale in wall-bounded turbulence.

In this study, as indicated in figure 1, particles can directly impact TKE transport through momentum coupling (Elghobashi & Truesdell 1993), thereby modulating specific scales of turbulent structures directly, i.e. VLSMs in the outer layer (through route 1 in figure 1) or LSMs in the inner layer. As discussed above, particle modulation of LSMs in the inner layer also has the possible effect that particle

feedback on LSMs near the wall can have upscale, indirect influences on VLSMs via nonlinear energy transfer (through route 2 in figure 1); see for example Toh & Itano (2005) and Lee & Moser (2019). To better understand particle modulation of LSMs in the inner layer, Wang & Richter (2019) further investigated small particles and their ability to enhance the LSM regeneration cycle (depending non-monotonically on particle inertia; see also Saffman (1962)), with the assumption that this was a route through which particles could modify even larger scales in high-Reynolds-number flow. Therefore, as a follow-up, and since to date computational costs have precluded particle-laden direct numerical simulations at sufficiently high Reynolds number, for the first time we examine the effects of a wide range of particle inertia on VLSMs in open channel flow at Reynolds numbers of $Re_\tau = 550$ and $Re_\tau = 950$.

2. Numerical parameters

Direct numerical simulations of the Eulerian flow are performed for an incompressible Newtonian fluid using the same numerical implementation as in Richter & Sullivan (2014) and Richter (2015). A pseudospectral method is employed in the periodic directions (streamwise x and spanwise z), and second-order finite differences are used for spatial discretization in the wall-normal (y) direction. We simulate pressure-driven open channel flow because it is characterized by features of both closed channel flow and a boundary layer (Nezu & Nakagawa 1993; Cameron, Nikora & Stewart 2017), while also exhibiting the signatures of VLSMs at a more computationally accessible domain size and Reynolds number. A no-slip condition is imposed on the bottom wall and a shear-free condition is imposed on the upper surface; such boundary conditions have been proven capable of capturing many of the phenomena (e.g. VLSMs) seen in experiments with shear-free upper boundaries (see Pan & Banerjee 1995, 1996; Adrian & Marusic 2012). We remark here that the inertial particles do not collect at the free surface in this study, which is also observed experimentally by Sumer & Oguz (1978) and numerically by Pan & Banerjee (1996). The solution is advanced in time by a third-order Runge–Kutta scheme. A single-sided stretched grid (fine grid close to the wall, coarse grid close to the free surface) is used in this study. Comparisons with a double-sided stretched grid (fine grid close to the wall and the free surface) and the simulations of Yamamoto, Kunugi & Serizawa (2001) at $Re_\tau = 200$ produce nearly identical mean velocity profiles, shown in figure 2(a), and turbulent intensity profiles, shown in figure 2(b). In addition, the one-dimensional u-spectra $\phi_{u'u'}(k_z) = \langle \hat{u}'(k_z)\hat{u}'^*(k_z) \rangle$ for the single-sided stretched and double-sided stretched grids are shown in figure 2(c,d). Both close to the wall ($y^+ = 14.3$; figure 2c) and in the near free-surface region ($y^+ = 189.2$; figure 2d), single-sided and double-sided stretched grids agree with each other.

Particle trajectories and suspension flow dynamics are based on the Lagrangian point-particle approximation where the particle-to-fluid density ratio $\rho_p/\rho_f \gg 1$ and the particle size is smaller than the smallest viscous dissipation scales of the turbulence. Only the Stokes drag force and two-way coupling have been incorporated since we restrict our study to low volume concentration $\overline{\Phi_V} = O(10^{-4})$ (see Balachandar & Eaton 2010). Gravitational settling is not considered in order to highlight the effect of the particle response time. Particles experience a purely elastic collision with the lower wall and upper rigid free surface. Two-way coupling is implemented via a particle-in-cell scheme, and has been validated against Capecelatro & Desjardins (2013) and Zhao et al. (2013) in turbulent channel flow. Grid convergence both of the flow and of the two-way coupling scheme have been verified as well (Gualtieri et al. 2013).

Type 1 ($Re_\tau = 550$)

$$N_x \times N_y \times N_z = 1024 \times 128 \times 512$$
$$L_x \times L_y \times L_z = 6\pi \times 1 \times 2\pi$$
$$L_x^+ \times L_y^+ \times L_z^+ = 10\,367 \times 550 \times 3456$$
$$\Delta x^+ \times \Delta y^+ (\text{wall, surface}) \times \Delta z^+ = 10.1 \times (1, 7.2) \times 6.75$$

Type 2 ($Re_\tau = 550$)

$$N_x \times N_y \times N_z = 2048 \times 128 \times 512$$
$$L_x \times L_y \times L_z = 12\pi \times 1 \times 2\pi$$
$$L_x^+ \times L_y^+ \times L_z^+ = 20\,734 \times 550 \times 3456$$
$$\Delta x^+ \times \Delta y^+ (\text{wall, surface}) \times \Delta z^+ = 10.1 \times (1, 7.2) \times 6.75$$

Type 3 ($Re_\tau = 950$)

$$N_x \times N_y \times N_z = 1024 \times 256 \times 512$$
$$L_x \times L_y \times L_z = 10.8 \times 1 \times \pi$$
$$L_x^+ \times L_y^+ \times L_z^+ = 10\,260 \times 950 \times 2984$$
$$\Delta x^+ \times \Delta y^+ (\text{wall, surface}) \times \Delta z^+ = 10 \times (1, 6.4) \times 5.8$$

Type	Case	$\overline{\Phi_m}$	ρ_p/ρ_f	$\overline{\Phi_v}$ ($\times 10^{-4}$)	N_p ($\times 10^6$)	τ_p	St^+	St_K (inner, outer)	St_{out}	$u_\tau T/h$
1	1	Single-phase flow								32
	2	0.024	16	15	12.6	0.51	2.42	0.587, 0.211	0.08	22
	3	0.14	160	8.75	7.33	5.1	24.2	5.87, 2.11	0.8	22
	4	0.14	400	3.5	2.93	12.7	60.5	14.7, 5.26	2.0	22
	5	0.14	1200	1.17	0.98	38.2	182	44.0, 15.8	6.0	22
	6	0.14	6000	2.33	0.195	191	908	220, 79	30	22
2	7	Single-phase flow								20
3	8	Single-phase flow								18
	9	0.14	1600	0.875	1.68	12.7	180.5	45.1, 12.8	4.1	18
	10	0.14	3200	0.438	0.84	25.5	361	90.3, 25.5	8.2	18

TABLE 1. Parameters of numerical simulations. The friction Reynolds number is $Re_\tau \equiv u_\tau h/\nu$, where h is the depth of the open channel and the particle relaxation time is $\tau_p \equiv \rho_p d^2/(18\rho_f \nu)$ where d is the particle diameter. The ratio d_p/η_K is maintained at a value of approximately 0.42. The particle Reynolds number remains $O(1)$ or lower. $\overline{\Phi_m}$ is the particle mass concentration and N_p is the total particle number. The superscript '+' is the dimensionless number based on viscous scale, where δ_ν, u_τ and ν/u_τ^2 correspond to the viscous length scale, velocity scale and time scale, respectively. St_K represents the dimensionless particle time scale based on averaged Kolmogorov time scale in the inner layer $y^+ < 100$ and outer layer $y^+ > 100$, corresponding to LSM and VLSM strong regions as shown in figure 8. St_{out} represents the dimensionless particle time scale based on the outer-flow time scale h/U_{bulk}, where U_{bulk} is the bulk velocity of the channel.

Particle modulation of turbulence is often characterized by the relative time scales between particles and local turbulent structures. The multiple turbulent structures spanning a wide spatial and temporal range (e.g. LSMs and VLSMs) result in a wide parameter space of the particle inertia to be investigated. As shown in table 1, we choose St^+ in the range of 2.42–908 based on the inner viscous time scale, which corresponds to St_{out} ranging from 0.08 to 30, where St_{out} is based on the outer bulk flow time scale h/U_{bulk}. This also corresponds to St_K in the range 0.587–220 based on the average Kolmogorov scale in the inner layer and 0.211–79 based on the average Kolmogorov scale in the outer layer. In single-phase channel flow,
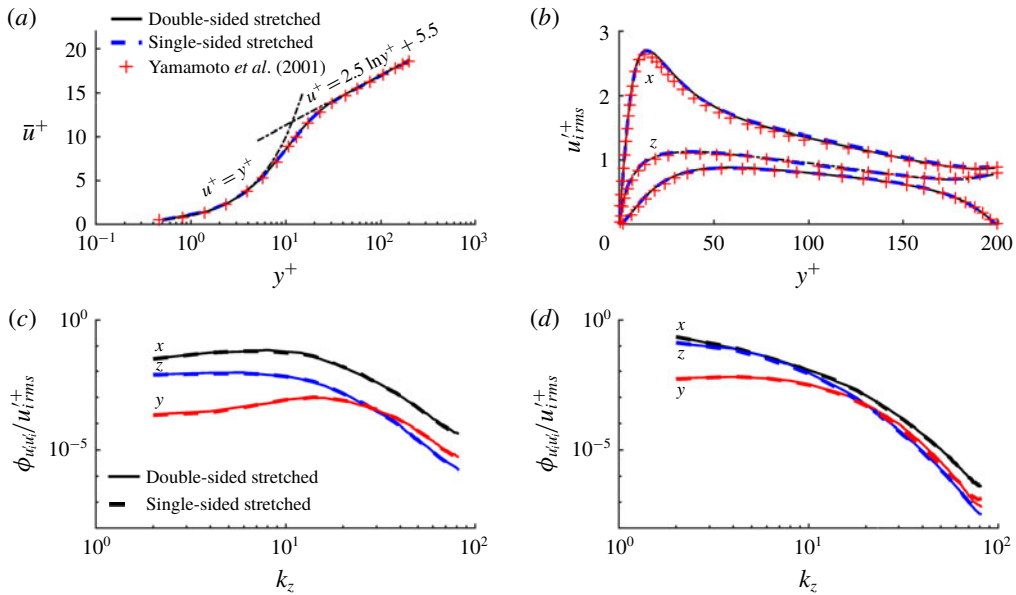
FIGURE 2. (Colour online) (*a*) Mean streamwise velocity profile. (*b*) Profiles of root-mean-square of velocity fluctuations. (*c*,*d*) Streamwise TKE spectra as a function of wavenumber in spanwise direction at two wall-normal heights: (*c*) close to the wall $y^+ = 14.3$ and (*d*) near the free-surface region $y^+ = 189.2$. Values in all panels are normalized by viscous scales.

del Álamo & Jiménez (2003) use $L_x \times L_z = 8\pi h \times 4\pi h$ at $Re_\tau = 550$ and Abe, Kawamura & Choi (2004) choose $L_x \times L_z = 12.8h \times 6.4h$ at $Re_\tau = 640$ to study VLSMs. In the current particle-laden flow, the domain size $L_x \times L_z = 6\pi h \times 2\pi h$ is used, slightly shorter than in del Álamo & Jiménez (2003) but larger than in Abe *et al.* (2004). With this domain size, we observe the appearance of a bimodal energy spectrum in the spanwise direction and compare well with del Álamo & Jiménez (2003) (see figure 8). In single-phase flow it is well known that VLSMs are very long in the streamwise direction, and fully capturing their extent is computationally expensive (Lozano-Durán & Jiménez 2014). Therefore as a test, case 7 doubles the streamwise extent for single-phase flow in order to check any effects of streamwise confinement on VLSMs by comparing to case 1 (the streamwise velocity spectrum in the spanwise direction is shown later in figure 8(*a*); negligible differences were observed). Cases 1–6 are then designed to investigate the effects of particle inertia by systematically increasing the particle Stokes number. In order to further examine particle direct modulation of VLSMs, cases 8–10 are performed at a higher $Re_\tau = 950$ for single-phase and particle-laden flow – these ultimately yield identical conclusions.

3. Results and discussion

3.1. *Particle distribution in two distinct layers*

Mean particle volume concentrations in the inner layer and outer layer are shown in figure 3(*a*), exhibiting a non-monotonic behaviour with Stokes number but with an opposite trend. In the inner layer it is maximized for case 3, which corresponds to $St^+ = 24.2$. At the same time, case 3 also exhibits the minimum in the outer
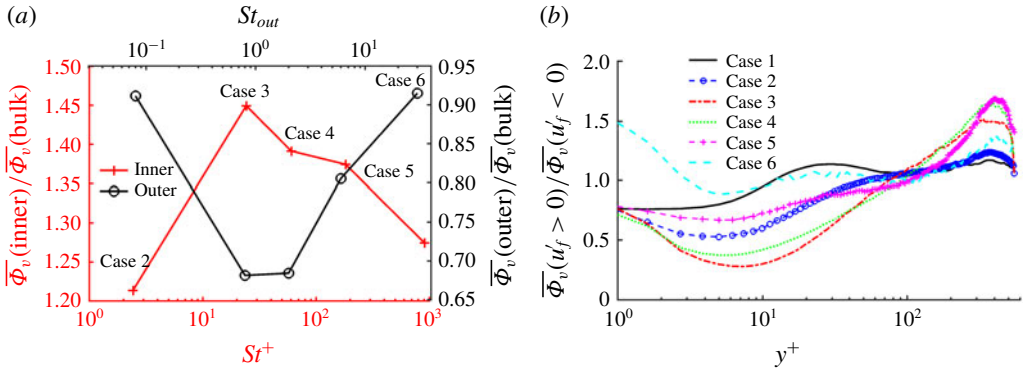
FIGURE 3. (Colour online) (*a*) The mean particle volume concentration in the inner layer (as a function of St^+) and outer layer (as a function of St_{out}), scaled by the bulk value. (*b*) The ratio between particle concentrations with $u'_f > 0$ and $u'_f < 0$. For single-phase flow (case 1), Eulerian grid points with $u' > 0$ or $u' < 0$ are plotted.

layer, where the more relevant Stokes number is $St_{out} = 0.8$. Stokes numbers lower or higher than case 3 result in fewer particles in the inner layer but more particles in the outer layer. This often-observed behaviour is due to turbophoresis (Reeks 1983), which induces a net particle flux towards the wall resulting in higher particle volume concentration in the inner layer than in the outer layer.

It is also commonly accepted that inertial particles preferentially accumulate in low-speed streaks (Pan & Banerjee 1996; Marchioli & Soldati 2002), which is also observed in this study. Particle numbers in 'upwelling' and 'downwelling' regions can be straightforwardly counted by testing whether $u'_f < 0$ or $u'_f > 0$, where u'_f is the fluid fluctuating velocity seen by the particle. Then, the ratio of the number of particles in 'upwelling' and 'downwelling' regions can be used to compare across different wall-normal locations and Stokes numbers. This ratio, cast in terms of the effective volume concentration corresponding to these particle counts, is shown in figure 3(*b*). Here, there is a clear non-monotonic trend with the Stokes number and with *y*. In the inner layer, there are more particles in the 'upwelling' fluid motions than in the 'downwelling' fluid motions, which is opposite compared to the outer layer. The lowest ratio appears for case 3 at $St^+ = 24.2$ in the inner layer, while the highest ratio appears for case 5 at $St_{out} = 6.0$ in the outer layer. Thus in the inner layer, relatively low-inertia particles collect in the low-speed streaks, while in the outer layer, higher-inertia particles collect in the high-speed regions. The relevant Stokes numbers are different for each, since the respective fluid time scales are different.

The relationship between particle distributions and the different turbulent structures (i.e. VLSMs and LSMs) is still poorly understood, however. To explore this, we introduce a mean fluid streamwise velocity fluctuation at the particle positions, but filtered according to the wavelengths associated with LSMs and VLSMs:

$$\overline{u'_{f\_p}}(\text{VLSMs}) \equiv \frac{\overline{\Phi_v u'_{\lambda_x > 5h, \, \lambda_z > 0.75h}}}{\overline{\Phi_v}}, \quad \overline{u'_{f\_p}}(\text{LSMs}) \equiv \frac{\overline{\Phi_v u'_{\lambda_x < 5h, \, \lambda_z < 0.75h}}}{\overline{\Phi_v}}. \quad (3.1a,b)$$

Here, the interpolated velocity u_f is projected onto the Eulerian grid, allowing for the u'_f field to be transferred to Fourier space ($\hat{u}'_f$). The goal is to artificially filter out targeted turbulent structures (e.g. removing wavelengths with $\lambda_x < 5h$, $\lambda_z < 0.75h$ to
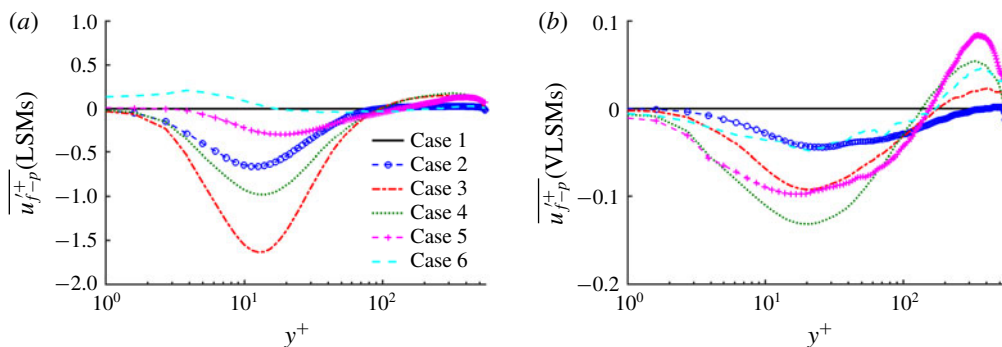
FIGURE 4. (Colour online) Mean fluid streamwise velocity fluctuation at particle locations defined in (3.1): (*a*) in LSMs ($\lambda_x < 5h$, $\lambda_z < 0.75h$) and (*b*) in VLSMs ($\lambda_x > 5h$, $\lambda_z > 0.75h$).

isolate VLSMs) in order to obtain u'_f contributed by specific turbulent structures. For single-phase flow, Φ_v is set to one at all Eulerian grid points and the same procedure is followed. These quantities are shown in figure 4. In the inner layer, $\overline{u'_{f\_p}}$ is negative in both VLSMs and LSMs, indicating that particles are more likely to reside in the large- and very-large-scale low-speed streaks compared to the high-speed streaks. The minimum values of $\overline{u'_{f\_p}}$ for LSMs (case 3 with $St^+ = 24.2$ in figure 4*a*) and VLSMs (case 4 with $St^+ = 60.5$ in figure 4*b*) appear at different Stokes numbers, again since the flow time scales associated with LSMs and VLSMs are different.

In the outer layer, $\overline{u'_{f\_p}}$ is positive for both VLSMs and LSMs, indicating that particles tend to reside in the 'downwelling' regions at the scales of both the LSMs and the VLSMs. The maximum value of $\overline{u'_{f\_p}}$ for VLSMs (figure 4*b*) appears for case 5 with $St_{out} = 6.0$. Comparing the inner layer with the outer layer, $\overline{u'_{f\_p}}$ for LSMs is considerably stronger in the inner layer than in the outer layer, as shown in figure 4(*a*). Two possible reasons may explain this. One is that the intensity of LSMs is much weaker in the outer layer than in the inner layer (which will be shown later in figure 9*a*); the other is that particle preferential concentration is not as strongly correlated with streaky motions in the outer layer as compared to the inner layer (which will be shown in figure 6*a*). However, for $\overline{u'_{f\_p}}$ in VLSMs (figure 4*b*), the magnitude is comparable between the inner layer and the outer layer, albeit with opposite preferred signs.

In terms of particle clustering behaviour, it is well established that, for wall-bounded turbulent flow in the inner layer, low-inertia particles ($St^+ < O(0.1)$) tend to distribute homogeneously in wall-normal planes (Pan & Banerjee 1996), while intermediate Stokes numbers ($St^+ = O(10)$) exhibit particle clustering in near-wall streaks (Marchioli & Soldati 2002; Sardina *et al.* 2012; Richter 2015; Wang & Richter 2019) and high-inertia particles ($St^+ > O(100)$) behave with ballistic trajectories (thus eliminating much of the clustering). This qualitative transition with St^+ is observed within the inner region of the simulated open channel flow. Figure 5(*a–e*) present isosurfaces of particle concentration (2.5 times the bulk $\overline{\Phi_v}$) for cases 2–6 in the inner and outer regions for increasing Stokes numbers. The advantage of showing concentration isosurfaces as opposed to individual Lagrangian points is that this method better visualizes the high-concentration particle clusters. The three panels across the horizontal represent three slabs at progressively increasing

wall-normal distances (at the same snapshot in time): layer 1, $30 < y^+ < 130$, layer 2, $150 < y^+ < 250$, and layer 3, $450 < y^+ < 550$.

Here we find particles accumulating in the inner-flow low-speed streaks at intermediate $St^+ = 24.2–60.5$ (cases 3 and 4 in layer 1 of figure 5*b,c*); this is similar to many other studies, as noted above. At the same time, a new type of organized structure in the outer flow region is observed. These are especially clear at higher Stokes numbers, e.g. $St^+ = 182$ ($St_{out} = 6$) for case 5 shown in layers 2 and 3 of figure 5(*d*). However, with a very high particle inertia, $St^+ = 908$ ($St_{out} = 30$), particles behave ballistically in the outer flow region as shown in layers 2 and 3 of figure 5(*e*), tending to distribute more homogeneously. These two distinct, non-monotonic particle accumulation behaviours in the inner and outer layers peak at different Stokes numbers ($St^+ = O(10)$ in the inner layer and $St_{out} = 6$ in the outer layer) and have a strong influence on the non-monotonic modulation of the VLSMs in the outer region via the two routes indicated in figure 1. This will be discussed further in §3.2.

In order to further quantify the particle clustering behaviour, we employ a Voronoï diagram analysis, which compares the distribution of the tessellation areas in the particle-laden cases with the expected Poisson distribution if the particles were randomly distributed (see e.g. Monchaux, Bourgoin & Cartellier 2012). A maximum clustering effect is typically observed for St_K around unity in isotropic turbulence (Monchaux *et al.* 2010; Baker *et al.* 2017) and buoyancy-driven wall-bounded turbulence (Park, O'Keefe & Richter 2018). Figure 6(*a,b*) show the standard deviation ($\sigma_\mathcal{V}$) of the distribution of the normalized Voronoï area $\mathcal{V} = A/\overline{A}$, where the inverse of the average Voronoï area $\overline{A}$ indicates the mean particle concentration. The $\sigma_\mathcal{V}$ value is scaled by the standard deviation of a random Poisson process (RPP; $\sigma_{RPP} = 0.52$). The ratio $\sigma_\mathcal{V}/\sigma_{RPP}$ exceeding unity indicates that particles are accumulating in clusters as compared to truly randomly distributed particles.

Figure 6(*a*) shows the ratio $\sigma_\mathcal{V}/\sigma_{RPP}$ for multiple heights across all Stokes numbers, while figure 6(*b*) shows the ratio as a function of St_K for two different representative heights ($y^+ = 50$ and $y^+ = 200$ are plotted based on St_K of the inner layer and outer layer, respectively, as provided in table 1). In the inner layer ($y^+ = 50$), from case 2 to case 6 ($St^+ = 2.42 - 908$ or $St_K = 0.58 - 220$), the clustering effect experiences a non-monotonic evolution as a function of Stokes number. The largest value appears at $St^+ = 24.2$ and it gradually decreases to unity with a higher Stokes number. This is similar to the result of the investigation of Wang & Richter (2019) that particles with $St^+ = 29.5$ preferentially accumulate in the streaks whereas higher-inertia particles tend to spread throughout the inner layer. With increasing wall-normal distance, the ratio $\sigma_\mathcal{V}/\sigma_{RPP}$ decreases at very low Stokes number (case 2) whereas it increases at higher Stokes numbers (cases 3–6). At still higher Stokes numbers (case 7), the ratio $\sigma_\mathcal{V}/\sigma_{RPP}$ again approaches unity. These very heavy particles cannot follow the streamlines, resulting in a nearly random particle distribution. In the outer layer ($y^+ = 200$), the largest value appears at $St_K = 2.11$ ($St_{out} = 0.8$), similar in magnitude to previous investigations of clustering in isotropic turbulence; peaks were found for $St_K = 3.0$ and $St_K = 1.0$ by Monchaux *et al.* (2010) and Baker *et al.* (2017), respectively.

3.2. *Particle modulation of TKE in LSMs and VLSMs*

The premultiplied, two-dimensional energy spectrum of streamwise velocity, $k_x k_z \Phi_{u'u'}$, where $\Phi_{u'u'} = \langle \hat{u}'(k_x, k_z, y)\hat{u}'^*(k_x, k_z, y) \rangle$, is shown in figure 7 for $Re_\tau = 550$ as a function of wall-normal distance ($\hat{u}'$ is the Fourier coefficient of u'). Figure 7 exhibits
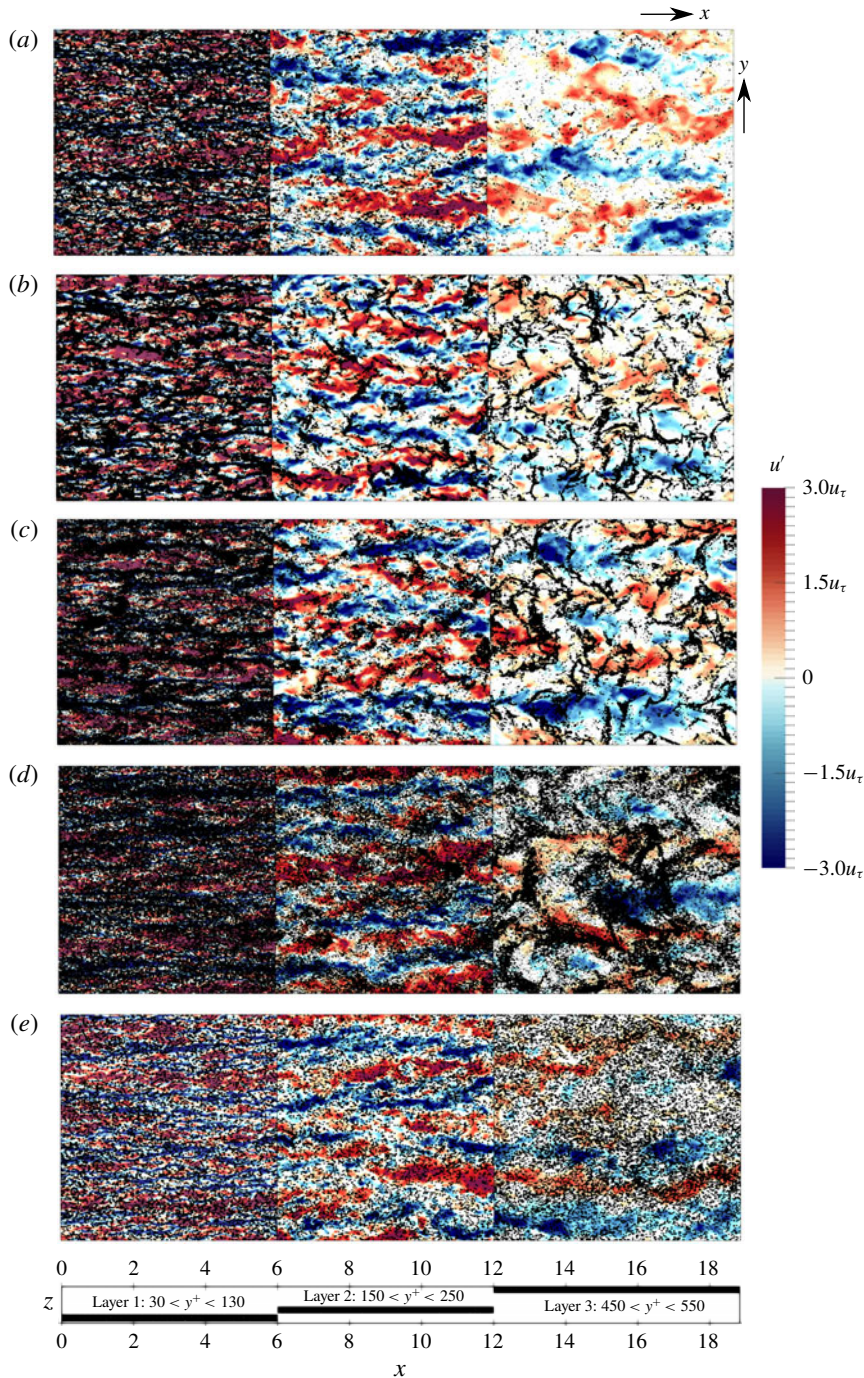
FIGURE 5. (Colour online) (a) Instantaneous streamwise velocity fluctuation u' (colour contours) in three x–z planes (panels from left to right: $y^+ = 50$, 150, 450) and isosurface of particle concentration (2.5 times bulk $\overline{\Phi_v}$) in three slabs (layer 1, $30 < y^+ < 130$, layer 2, $150 < y^+ < 250$, and layer 3, $450 < y^+ < 550$). Panels (a–e) refer to cases 2–6, respectively. A supplementary movie is available online at https://doi.org/10.1017/jfm.2019.210.
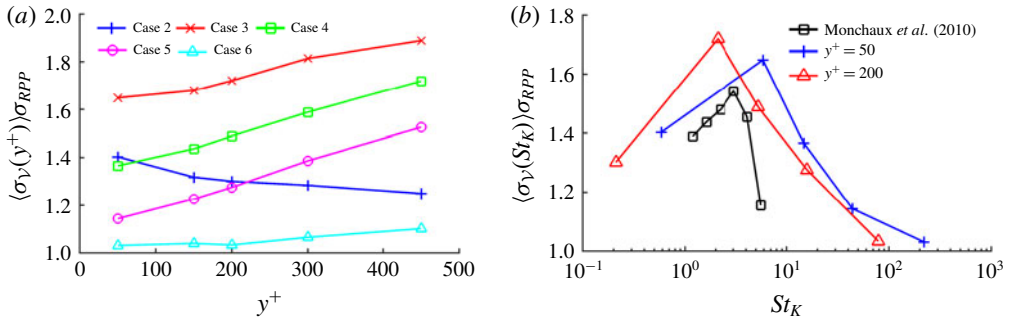
FIGURE 6. (Colour online) Standard deviation of the normalized Voronoï area $\sigma_{\mathcal{V}}$, normalized by that of a random Poisson process, σ_{RPP}: (*a*) as a function of height in wall-normal direction of five Stokes numbers and (*b*) as a function of St_K at two wall-normal locations ($y^+ = 50$ and $y^+ = 200$ are plotted based on St_K of the inner layer and outer layer as in table 1). Experimental results of an isotropic turbulence from Monchaux, Bourgoin & Cartellier (2010) are also shown.

a 'boot-shaped' structure, particularly well defined for case 2 (figure 7*b*) and case 5 (figure 7*e*). The 'forefoot' corresponds to the LSMs in the near-wall region, whereas the 'bootleg' corresponds to the VLSMs. The signature of VLSMs indeed appears at the upper-left corner (long and wide wavelengths in the streamwise and spanwise directions) for single-phase flow in figure 7(*a*). This VLSM signature is nearly unchanged for case 3 and case 6 whereas it is slightly weakened in case 4. It is clear, however, that for low Stokes number ($St^+ = 2.42$ of case 2 in figure 7*b*) and high Stokes number ($St_{out} = 6$ of case 5 in figure 7*e*), energy contained by the VLSMs is enhanced by the presence of particles. In addition to the enhanced VLSMs observed in the outer layer, the large-scale energetic structures (e.g. the 'bootleg' within $y^+ < 100$ in figure 7*b,e*) extend into the inner layer, which are referred to as deep *u*-modes (del Álamo & Jiménez 2003) or VLSM 'footprints' (Hutchins & Marusic 2007), and are a possible path for the inverse scale transfer from LSMs to VLSMs found by Lee & Moser (2019).

Figure 8 displays as a function of y^+ the premultiplied, one-dimensional *u*-spectra $k_z \phi_{u'u'}(k_z)$, where $\phi_{u'u'}(k_z) = \langle \hat{u}'(k_z)\hat{u}'^*(k_z) \rangle$, as a function of the normalized spanwise wavelength λ_z^+. As a reference, we compare with the results of del Álamo & Jiménez (2003) for wall-bounded channel flow at the same $Re_\tau = 550$, who find that the turbulence in the outer flow behaves roughly isotropically if VLSMs are artificially removed (i.e. VLSMs introduce anisotropy). Comparing del Álamo & Jiménez (2003) (who filter out high wavelengths, so $k_z\phi_{u'u'}(k_z)$ with only $\lambda_x < 5h$ are plotted) and the present (unfiltered) simulation in figure 8(*a*), we observe that, for unladen flow, with or without the contribution from turbulent structures of $\lambda_x > 5h$, the spectral signature of LSMs is hardly affected (see the spectrum below $y^+ = 100$ with $\lambda_z^+ < 200$) (Jiménez & Pinelli 1999). As noted previously, any effect of a limited streamwise domain extent L_x is minimal, since figure 8(*a*) shows that the energy contained in VLSMs in a short domain (contour represents for case 1) is nearly identical to the long domain (case 7 is shown by lines). Thus overall our unladen simulations are consistent with the current understanding of VLSMs. We point out that in single-phase flow, only (0.2, 0.4, 0.8) times the maximum value based on the single-phase flow are displayed in figure 8(*a*); therefore the second peak in the outer layer is not as readily observed
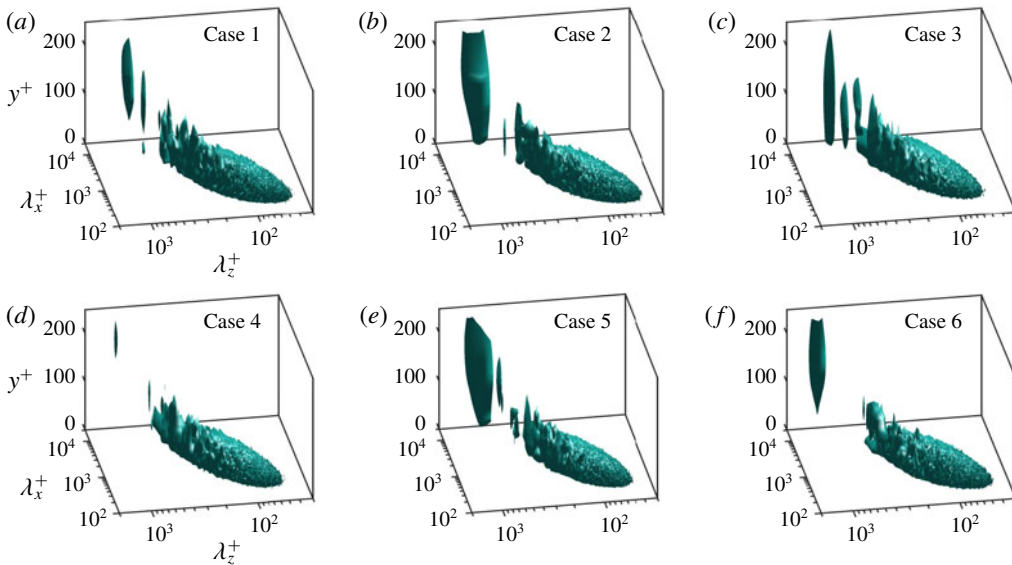
FIGURE 7. (Colour online) Premultiplied two-dimensional energy spectrum $k_x k_z \Phi_{u'u'}/u_\tau^2$ as a function of λ_x and λ_z and the wall-normal direction y. An isosurface of 0.1 times the maximum value of the single-phase flow is illustrated. Panels $(a–f)$ refer to cases 1–6, respectively.

as in figure 7(a). For case 2 (figure 8b) and case 5 (figure 8e), the contribution from VLSMs forms a bimodal spanwise spectrum at $600 < \lambda_z^+ < 1000$ ($h < \lambda_z < 2h$) at heights above the inner layer. The enhancement of the VLSM signature is also found at $Re_\tau = 950$, $St_{out} = 8.0$ as shown in figure 8($g–i$) for cases 8–10. The Stokes number based on the outer time scale for case 9 is similar to that of case 5 at $Re_\tau = 550$. By investigating inertial particle modulation of the regeneration cycle of LSMs, Wang & Richter (2019) found that particle inertia has a non-monotonic effect on LSMs in the inner region: low inertia ($St^+ = O(1)$, e.g. $St^+ = 2.42$ of case 2) promotes the regeneration cycle whereas high inertia ($St^+ = O(10)$, i.e. $St^+ = 24.2 − 182$ of cases 3–5) attenuates the regeneration cycle. However, we see from figure 8 that VLSM enhancement occurs at both low and high Stokes numbers (i.e. case 2 and case 5).

In order to quantify the TKE of VLSMs and LSMs modulated by particles and to demonstrate their effect as a function of Stokes number, we show $k_{u'u'} \equiv \overline{u'u'}$ for LSMs (represented by $\lambda_x < 5h$) and VLSMs (represented by $\lambda_x > 5h$) in figure 9(a) and (b), respectively. The TKE of LSMs is 4–5 times larger than the TKE of VLSMs. The $k_{u'u'}$ contributed by LSMs and VLSMs is shown as a function of Stokes number for the representative inner-layer height $y^+ = 15$ in figure 9(c) and the representative outer-layer height $y^+ = 157$ in figure 9(d). Figure 9(c) shows that, in the inner layer, the minimum TKE of LSMs appears for case 3 ($St^+ = 24.2$), corresponding to the strongest turbulence attenuation observed by Wang & Richter (2019). In the outer layer, the minimum TKE of LSMs appears at a higher Stokes number, i.e. case 5 ($St_{out} = 6.0$). However, the TKE modulation of VLSMs is distinct from, and even opposite in behaviour to, that of LSMs. As shown in figure 9(c), in the inner layer, the intensity of VLSMs reaches its maximum for case 3 ($St^+ = 24.2$) whereas the TKE of VLSMs has two peaks in the outer layer: case 2 ($St_{out} = 0.08$) and case 5 ($St_{out} = 6.0$).
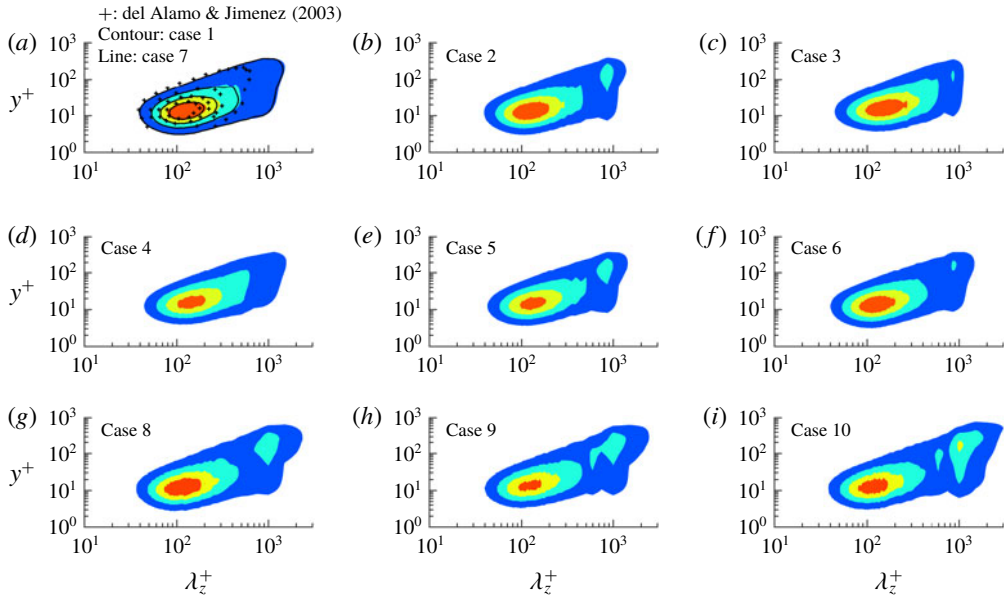
FIGURE 8. (Colour online) Premultiplied one-dimensional u-spectra as functions of spanwise wavelength and wall-normal direction. The contours are 0.2, 0.4, 0.8 times the maximum value based on the single-phase flow. Panels (a–f) are for cases 1–6 at $Re_\tau =$ 550; and panels (g–i) are for cases 8–10 at $Re_\tau = 950$. In (a), the shaded contours are for case 1 and line types represent case 7, which doubles the domain size of case 1 in the streamwise direction. The '+' symbols denote isolines of (0.2, 0.4, 0.8) from del Álamo & Jiménez (2003), containing modes only with $\lambda_x < 5h$ (VLSMs with $\lambda_x > 5h$ are artificially removed).

As argued below, these two peaks correspond to indirect and direct modulation mechanisms, respectively, and will be discussed in § 3.3.

Additional qualitative evidence of VLSM enhancement can be seen in figure 10, which provides a representative snapshot of the streamwise velocity fluctuation in the x–z plane at $y^+ = 157$. Comparing the snapshots in figure 10(c,e) and figure 10(a), it may not be easy to detect VLSM modulation. However, when the flow field is filtered by a threshold $\lambda_x > 10h$ and $\lambda_z > 0.75h$, as displayed in figure 10(b,d,f), it is evident that VLSMs are stronger and more coherent in case 2 (figure 10d) and case 5 (figure 10f) as compared to single-phase flow. This is a more qualitative confirmation of the results shown in figures 7, 8 and 9. We now turn our investigation to understanding why the VLSM modulation appears to have two distinct peaks in Stokes number – in particular, demonstrated by case 2 and case 5.

3.3. *Two mechanisms of VLSM enhancement by particles*

In order to verify the above hypothesis that the VLSM enhancement in case 2 is due to particle modulation of LSMs in the inner flow (we refer to this as indirect modulation of VLSMs) whereas in case 5 it is due to the particle direct modulation on the VLSMs in the outer flow, we perform a conditional numerical test to identify the particles' effective region of influence regarding VLSM enhancement by artificially applying the particle feedback force separately in only one of three locations: (1) the
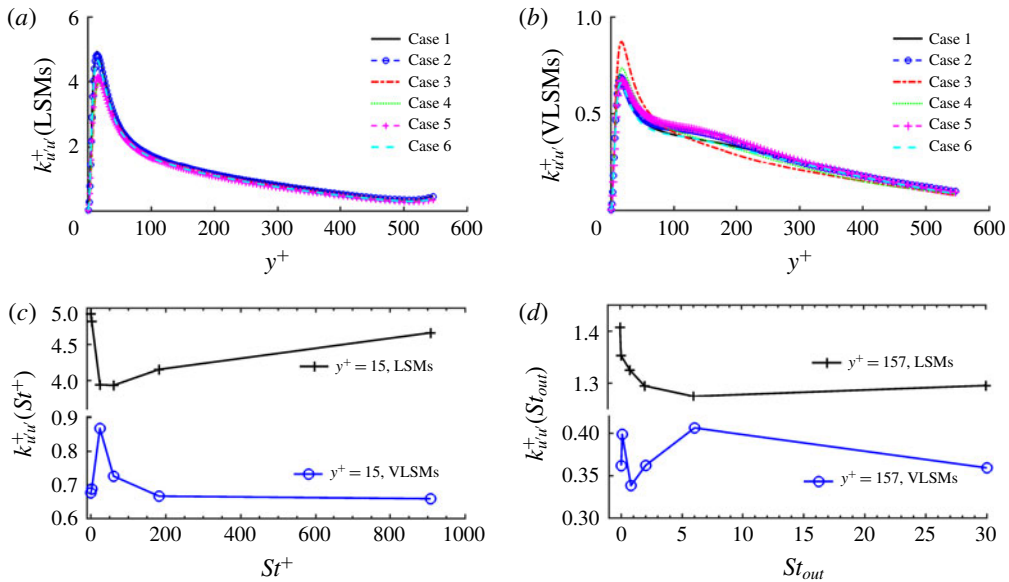
FIGURE 9. (Colour online) Streamwise TKE ($k_{u'u'}$) contributed by (*a*) LSMs, $\lambda_x < 5h$, and (*b*) VLSMs, $\lambda_x > 5h$, of cases 1–6. Here $y^+ = 15$ and $y^+ = 157$ are used to represent the inner layer and outer layer, respectively. The corresponding value of $k_{u'u'}$ at the two heights is plotted against (*c*) St^+ and (*d*) St_{out}.
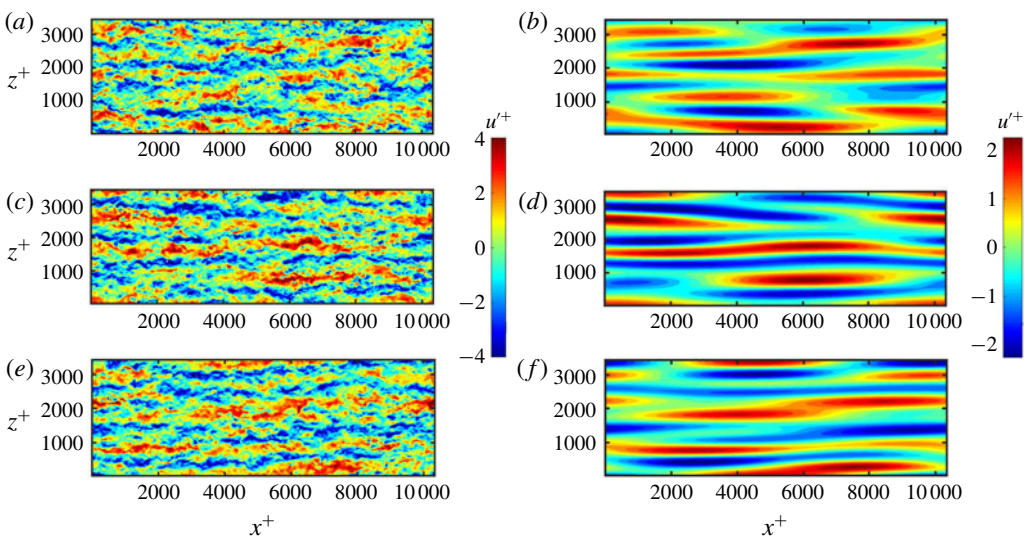

FIGURE 10. (Colour online) Instantaneous contours of streamwise velocity fluctuation scaled by u_τ on a wall-parallel plane at $y^+ = 157$ at the same time step. Panels (*a*,*c*,*e*) contain all modes; panels (*b*,*d*,*f*) are for the same flow field but only associating with VLSMs, containing modes with $\lambda_x > 10h$, $\lambda_z > 0.75h$ ($\lambda_x^+ > 5500$, $\lambda_z^+ > 412$). (*a*,*b*) Case 1; (*c*,*d*) case 2; and (*e*,*f*) case 5.
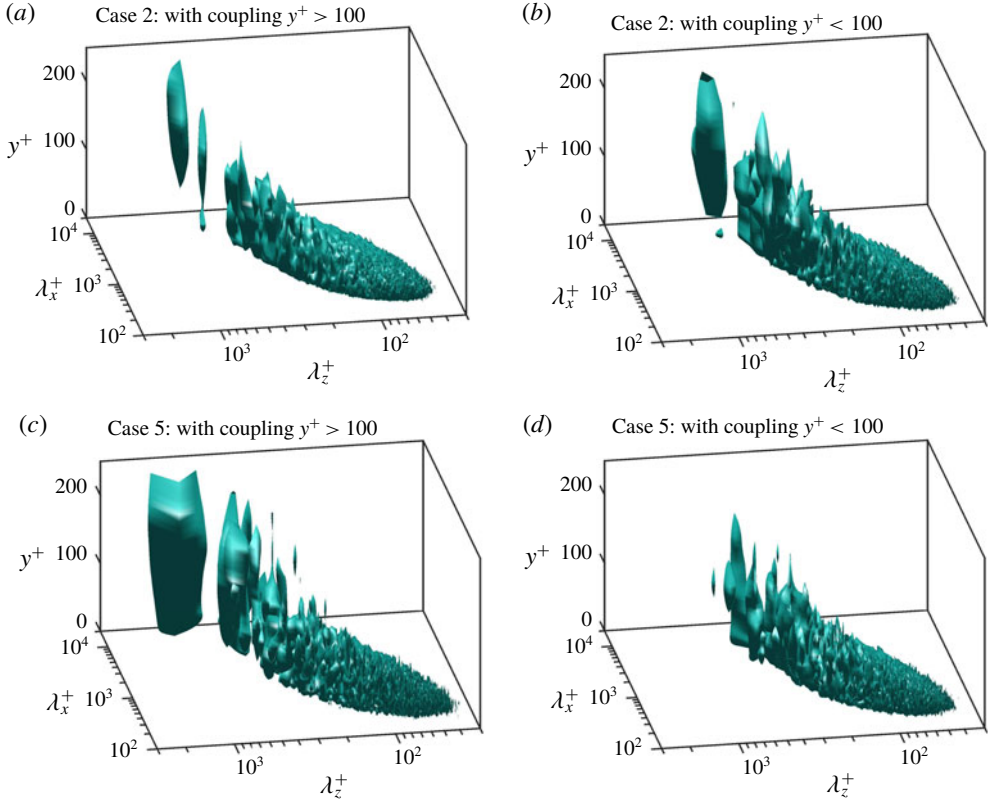
FIGURE 11. (Colour online) Premultiplied two-dimensional spectrum $k_x k_z \Phi_{u'u'}/u_\tau^2$ as a function of λ_x and λ_z in the wall-normal direction y. An isosurface of 0.1 times the common maximum value based on the single-phase flow is illustrated. (*a*,*c*) Only with particle coupling in the outer flow for case 2 and case 5. (*b*,*d*) Only with particle coupling in the regeneration cycle region for case 2 and case 5.

viscous sublayer ($y^+ < 15$), (2) the regeneration cycle region ($15 < y^+ < 100$), or (3) the outer flow ($y^+ > 100$). The premultiplied two-dimensional energy spectrum of streamwise velocity $k_x k_z \Phi_{u'u'}$ is shown in figure 11 as a function of y^+. Compared with figure 7(*a*), it can be seen that the VLSMs only experience enhancement in case 2 when particle coupling is included in the regeneration cycle region. For case 5, on the other hand, the opposite is true: VLSM enhancement is found only when particle coupling effects are included in the outer region. Both of these effects are observed throughout the entire range of y^+. The tests of two-way coupling applied for $y^+ < 15$ are not shown, but we find the spectrum in the range $3.77h < \lambda_x < 6.28h$ ($2073 < \lambda_x^+ < 3454$) and $0.78h < \lambda_z < 1.0h$ ($429 < \lambda_z^+ < 550$) is stronger than in the single-phase flow, but shorter and narrower than the streamwise and spanwise scale of the second peak of the TKE spectrum.

In spectral space, the modulation of LSMs and VLSMs by a dispersed phase is at least partially related to the direct influence on velocity fluctuations, which in turn can modify the production of TKE and/or Reynolds shear stress. This is demonstrated in figure 12, where we present the $\overline{u'u'}$ spectral production term $\hat{P}_{11} = -\langle \hat{u}'(k_z, y)\hat{v}'^*(k_z, y)\rangle\, \mathrm{d}U/\mathrm{d}y$ as well as the $\overline{u'v'}$ spectral production term
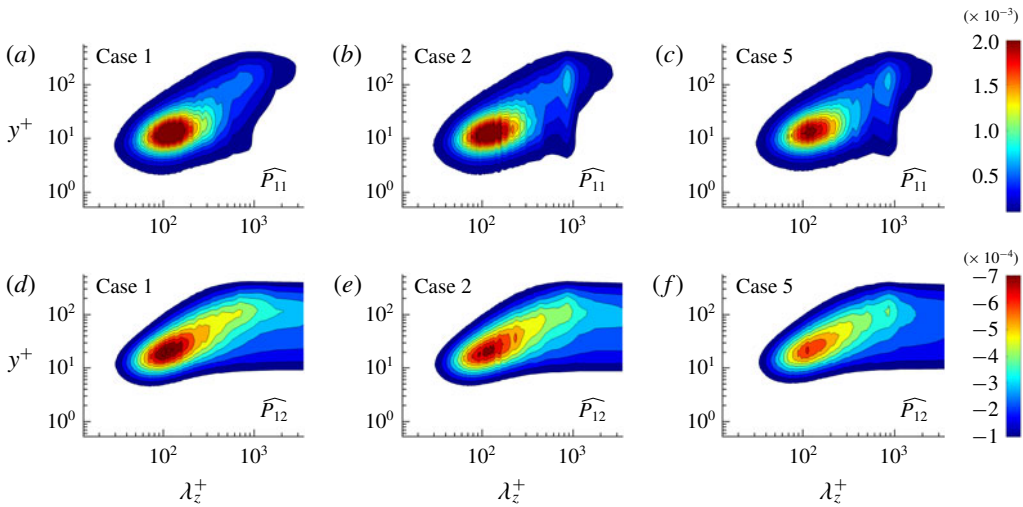
FIGURE 12. (Colour online) Production contribution to the streamwise TKE budget and Reynolds shear stress budget in spectral space normalized by u_τ^3/δ_ν: (a–c) $\hat{P}_{11}$ and (d–f) $\hat{P}_{12}$; (a,d) case 1, (b,e) case 2 and (c,f) case 5.

$\hat{P}_{12} = -\langle \hat{v}'(k_z, y)\hat{v}'^*(k_z, y)\rangle \, \mathrm{d}U/\mathrm{d}y$ as functions of λ_z^+ and the wall-normal direction y^+ for two different Stokes numbers both previously seen to enhance VLSMs: the low-Stokes-number case 2 and high-Stokes-number case 5. These are shown in comparison with single-phase flow case 1. Throughout the wall-normal direction, $\hat{P}_{11}$ is positive whereas $\hat{P}_{12}$ is negative. Comparing figures 12(a–c) with figures 8(a,b,e), respectively, we find that they have a similar overall shape, and the bimodal spectrum appears both in the premultiplied u-spectra as well as the production term $\hat{P}_{11}$, which is enhanced in case 2 and case 5 in comparison with the single-phase flow. In regards to $\hat{P}_{12}$, a similar overall shape as compared to premultiplied uv-cospectra (figure not shown) is observed even though the bimodal spectrum is not as obviously established as that for $\hat{P}_{11}$. The intensity of $\hat{P}_{12}$ ($\hat{P}_{12}$ is negative in the domain) is weakened in case 2 and case 5 in comparison with the single-phase flow by the presence of particles. Thus figure 12 indicates that production of $\overline{u'u'}$ is enhanced at the heights and wavenumbers associated with VLSMs, while at the same time, particularly for case 5, the production of Reynolds shear stress is diminished at the same wavelengths and heights.

In addition to the modifications to streamwise TKE and Reynolds shear stress production, particles can also act as a direct source/sink in the spectral TKE and Reynolds stress budgets. In the spectral energy budget, particle sources to the $\overline{u'u'}$ budget are denoted as $\hat{\Psi}_{11} = \mathrm{Re}\langle \hat{F}_x'(k_z, y)\hat{u}'^*(k_z, y)\rangle$ and to the $\overline{u'v'}$ budget as $\hat{\Psi}_{12} = \mathrm{Re}\langle \hat{F}_x'(k_z, y)\hat{v}'^*(k_z, y) + \hat{F}_y'(k_z, y)\hat{u}'^*(k_z, y)\rangle$, where Re stands for the real part and $\hat{F}$ is the Fourier transform of the particle coupling force. The mean value of $\Psi_{11} = \overline{F_x'u'}$ and $\Psi_{12} = \overline{F_x'v'} + \overline{F_y'u'}$ (where F_i', $i = x, y, z$, is the fluctuation of the particle feedback force on the carrier phase) in the inner layer and outer layer of all modes normalized by the bulk mass fraction Φ_m, is shown in figure 13(a) and figure 14(a), respectively. In both the inner layer and outer layer, the sign of Ψ_{11} is positive for case 2 whereas it becomes negative for cases 3–6. This is opposite when compared
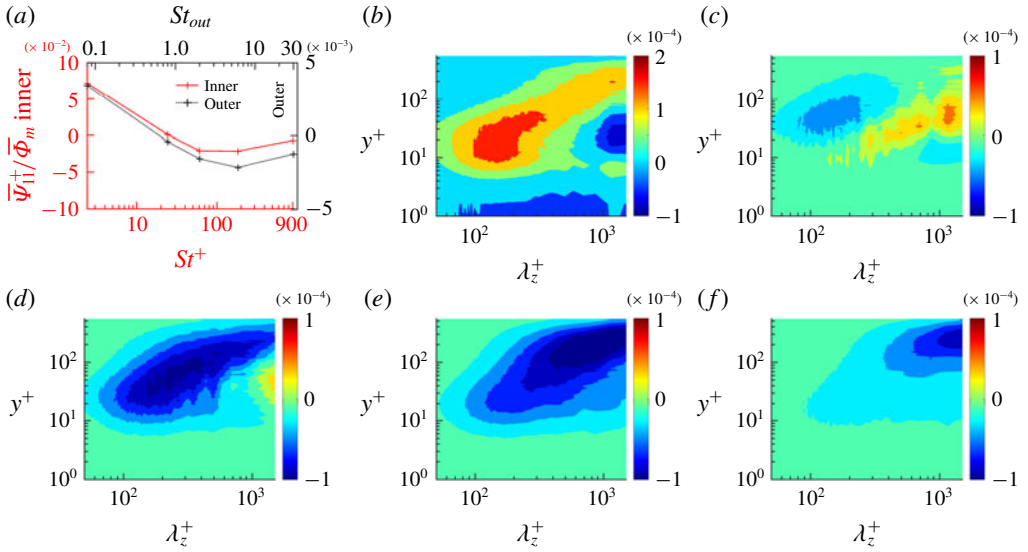
FIGURE 13. (Colour online) Particle feedback term Ψ_{11} contribution to the streamwise TKE budget. (*a*) Mean value of all modes in the inner and outer layers as a function of Stokes number, normalized by u_τ^3/δ_ν and bulk mass fraction $\overline{\Phi_m}$. (*b*–*f*) Contribution of $\hat{P}_{11}$ in spectral space of cases 2–6 as functions of spanwise wavelength and wall-normal direction, normalized by u_τ^3/δ_ν and local mass fraction $\overline{\Phi_m}(y)$.
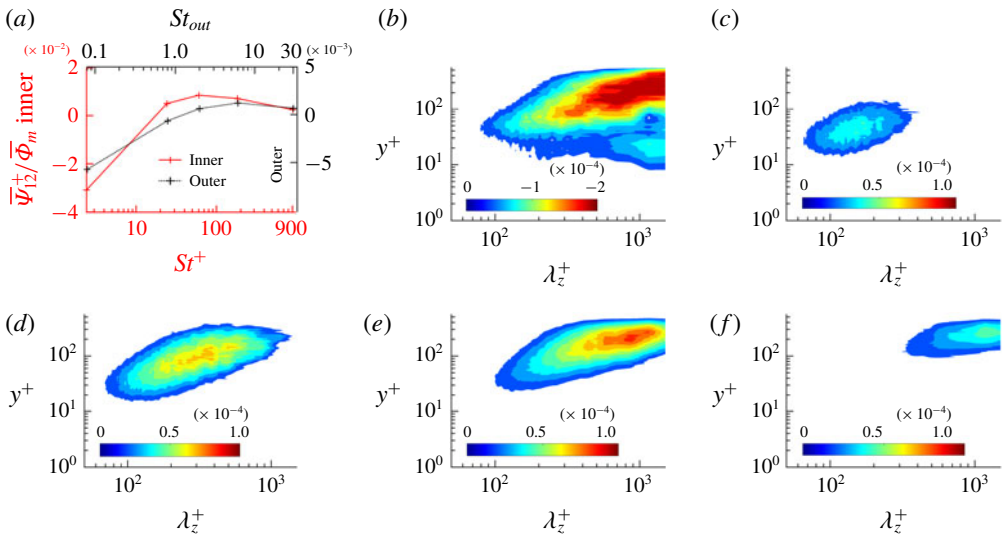

FIGURE 14. (Colour online) Particle feedback term Ψ_{12} contribution to the Reynolds shear stress budget. Figure legend is the same as figure 13.

to Ψ_{12}, indicating that Ψ_{11} and Ψ_{12} play opposite roles in the streamwise TKE budget and Reynolds stress budgets for the same Stokes number. In the spectral energy budget, the particle source to the $\overline{u'u'}$ budget is denoted by $\hat{\Psi}_{11}$ and to the $\overline{u'v'}$ budget

by $\hat{\Psi}_{12}$ (both normalized by local particle mass fraction Φ_m in figures 13 and 14). With increasing Stokes number as shown in figure 13(*b–f*) and figure 14(*b–f*), the regions of the highest magnitudes of $\hat{\Psi}_{11}$ and $\hat{\Psi}_{12}$ shift from the inner layer to the outer layer, and at the same time from low to high wavelength. In particular, it is found that, for case 2, a region of large positive $\hat{\Psi}_{11}$ (figure 13*b*) appears in the inner layer with wavelengths associated with LSMs, whereas in case 5, a region of large positive $\hat{\Psi}_{12}$ region instead develops at wavelengths associated with VLSMs (figure 14*e*). In contrast, case 2 exhibits a negative source of $\hat{\Psi}_{12}$ at these wavelengths (figure 14*b*), but for case 5 there is at the same time a noticeable change in the sign of the contribution and location of $\hat{\Psi}_{11}$ (figure 13*e*). This picture is consistent with the conditional tests, i.e. case 2 works with LSMs in the inner layer whereas case 5 works with VLSMs in the outer layer. This nearly opposite behaviour indicates that there might be two underpinning mechanisms of VLSM enhancement induced by low- and high-Stokes-numbers particles.

In particle-laden flow, Richter (2015) finds that the particle-induced, Stokes-number-dependent source/sink of TKE varies with wavelength, and is possibly associated with the particle clusters themselves (Capecelatro *et al.* 2018). Focusing exclusively on the inner region, Wang & Richter (2019) find that low-inertia particles enhance LSMs whereas high-inertia particles attenuate LSMs, which can help explain the positive particle feedback $\hat{\Psi}_{11}$ for case 2 (figure 13*b*) but negative for case 5 (figure 13*e*). In addition, as shown in figure 14(*b*), the particle source $\hat{\Psi}_{12}$ in case 2 always attenuates the generation of $\overline{u'v'}$. Therefore, in case 2, the positive feedback $\hat{\Psi}_{11}$ in the inner region is the most likely mechanism responsible for the enhancement of VLSMs in the outer region. This process of particles inducing upscale energy transfer (or a reverse cascade), tending to build up the energy level at high wavelengths due to the modulation of small-scale turbulent motions, is also observed in homogeneous turbulence (see Elghobashi & Truesdell 1993; Carter & Coletti 2018) and in turbulent Couette flow (see Richter 2015).

At low Stokes number ($St^+ = O(1)$), Klinkenberg *et al.* (2013) found that the disturbance energy needed to induce turbulence is low at small mass fractions (i.e. $\overline{\Phi_m} = 0.02$–0.06), whereas it is high at large mass fraction (i.e. $\overline{\Phi_m} = 0.138$), indicating a subtle dependence of two-way coupling effects on mass fraction at low Stokes number. In the current context, this understanding can be used to better interpret and understand the indirect modulation of VLSMs by low-Stokes-number particles. Figure 15 shows one-dimensional *u*-spectra $k_z \phi_{u'u'}(k_z)$ with increasing mass fraction ranging from $\overline{\Phi_m} = 1.2 \times 10^{-2}$ to 12×10^{-2}, all compared with the unladen flow. We observe that the modulation of VLSMs as a function of mass fraction is consistent with the behaviour shown by Klinkenberg *et al.* (2013): VLSMs are slightly enhanced by a small mass fraction of low-Stokes-number particles ($\overline{\Phi_m} = 1.2 \times 10^{-2}$ in figure 15*b*) and significantly promoted by increasing the mass fraction to $\overline{\Phi_m} = 2.4 \times 10^{-2}$ (figure 15*c*). With further increases in mass fraction, however ($\overline{\Phi_m} = 12 \times 10^{-2}$ in figure 15*d*), this enhancement begins to diminish. Again, the non-monotonic response of LSM regeneration found in Klinkenberg *et al.* (2013) and Wang & Richter (2019) appears to be linked to the underlying non-monotonic response of VLSM enhancement to low-Stokes-number particles.

Finally, in contrast to case 2, it is more straightforward to understand the VLSM modulation in case 5. As shown in figure 14(*e*), throughout the whole domain we observe that $\hat{\Psi}_{12}$ for case 5 always has a positive contribution to the $\overline{u'v'}$ budget and is at the same spatial locations as the VLSMs of the *u*-spectra (seen also at
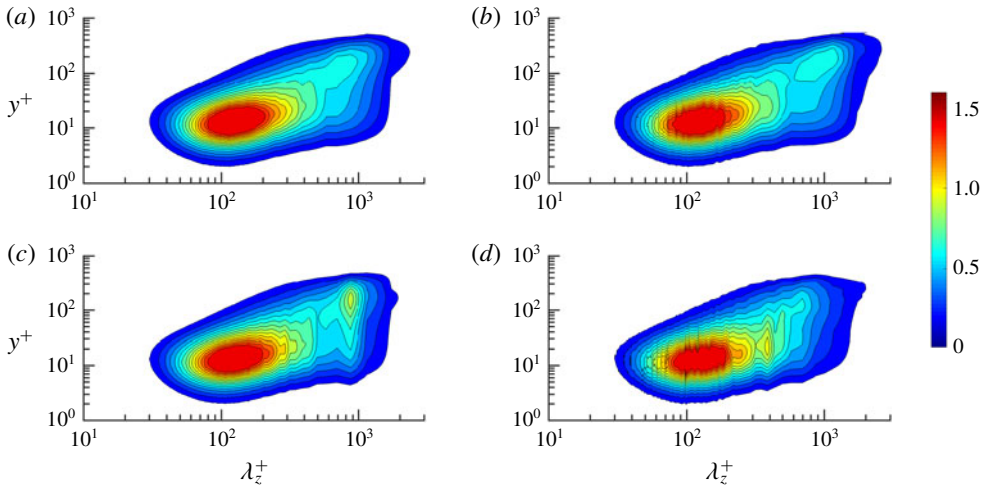
FIGURE 15. (Colour online) Premultiplied one-dimensional u-spectra as functions of spanwise wavelength and wall-normal direction, normalized by u_τ^2. (*a*) Single-phase flow case 1. (*b,d*) Stokes number $St^+ = 2.42$ of case 2 with three mass fractions: (*b*) $\overline{\Phi_m} = 1.2 \times 10^{-2}$, (*c*) $\overline{\Phi_m} = 2.4 \times 10^{-2}$, and (*d*) $\overline{\Phi_m} = 14 \times 10^{-2}$.

$Re_\tau = 950$ in case 9; figure not shown). On the other hand, $\hat{\Psi}_{11}$ for case 5 in figure 13(*e*) tends to suppress the generation of $\overline{u'u'}$. This ultimately results in $\hat{\Psi}_{12}$ exerted in the outer region as being the most likely explanation for the enhancement of VLSMs. As the source of Reynolds shear stress $-\overline{u'v'}$, the 'upwelling' and 'downwelling' cycles at very large scales (Adrian & Marusic 2012) are directly enhanced by the presence of high-inertia particles ($St_{out} = 6$ of case 5 at $Re_\tau = 550$ and $St_{out} = 8.2$ of case 10 at $Re_\tau = 950$) in the outer flow. These very large upwelling/downwelling structures further extract energy from the mean flow by working with local mean shear, as the production of streamwise turbulent kinetic energy budget ($P_{11} = -\overline{u'v'}\,dU/dy$); see for example the physical explanation in Nezu (2005).

4. Conclusions

In this paper, we have studied the effect of inertial particles on very-large-scale motions (VLSMs) in moderate Reynolds number in open channel flow. Higher particle concentrations are observed in the inner layer than the outer layer due to the towards-wall particle flux induced by turbophoresis. The particle concentration has a non-monotonic dependence on Stokes number whereas the trend is opposite between the inner layer and outer layer. In the inner layer, the particles are characterized by well-known preferential accumulation patterns in the anisotropic large-scale motions (LSMs), especially in low-speed streaks, and this behaviour scales as St^+ based on inner units. However, with increasing wall-normal distance, additional clustering structures are formed in the outer flow. The clustering behaviour is found to be dependent on St_K based on the local Kolmogorov scale, similar to the traditional picture described in isotropic turbulence. In addition, while particles preferentially accumulate in 'upwelling' LSMs within the inner layer (especially at $St^+ = 24.2$ in case 3), in the outer layer they cluster both in 'upwelling' and 'downwelling'

VLSMs (especially at $St_{out} = 6.0$ in case 5). The distinct bulk concentration and clustering behaviour in the two layers are non-monotonically dependent on Stokes number, thereby influencing two-way coupling. This is observed primarily in spectral analysis, where we observe that inertial particles have a non-monotonic effect on the VLSM modulation: low- and high-inertia particles both strengthen the VLSMs but the intermediate-inertia particles hardly affect their structure and energy.

By utilizing a conditional numerical test, we demonstrate there are two distinct routes through which inertial particles enhance the VLSMs in the outer layer. Low-inertia ($St^+ = 2.42$ based on the inner scale) particles strengthen the VLSMs due to the enhancement of the LSMs in the inner flow. On the contrary, high-inertia ($St_{out} = 6.0, 8.2$ based on the outer scale) particles strengthen the VLSMs due to direct interaction in the outer flow. The most direct route of particle modulation of turbulent motions comes from the particle feedback source in the turbulent energy budget. Correspondingly, we find that low-inertia particles have a positive $\hat{\Psi}_{11}$ in the inner flow and a negative $\hat{\Psi}_{12}$ in the outer flow, which is opposite to high-inertia particles. While the relationship between near-wall LSMs and the outer-scale VLSMs remains a subject of investigation, this suggests that there can exist an upscale transport of energy possible from LSMs to VLSMs. Inspired by previously observed, non-monotonic modulation of turbulence of low-inertia particles in the inner layer with varying mass fraction (Klinkenberg *et al.* 2013), we observe a VLSM modulation pattern with respect to mass fraction in the outer layer which coincides with the turbulence instability response in the inner layer. This is consistent with Toh & Itano (2005), who show numerically that LSMs and VLSMs interact in a co-supporting cycle, Marusic, Mathis & Hutchins (2010), who observe experimentally the high degree of velocity fluctuation correlation between the outer flow with the low-frequency content of the inner flow, and Lee & Moser (2019), who describe an inverse scale transfer from LSMs to VLSMs close to the wall. In contrast, high-inertia particles modulate the VLSMs directly, indicated by the particle feedback effect on the Reynolds shear stress budget with the same scale of VLSMs at the same spatial locations.

Acknowledgements

Supplementary movie

Supplementary movie is available at https://doi.org/10.1017/jfm.2019.210.

REFERENCES

ABE, H., KAWAMURA, H. & CHOI, H. 2004 Very large-scale structures and their effects on the wall shear-stress fluctuations in a turbulent channel flow up to $Re_\tau = 640$. *Trans. ASME J. Fluids Engng* **126** (5), 835–843.

ADRIAN, R. J. & MARUSIC, I. 2012 Coherent structures in flow over hydraulic engineering surfaces. *J. Hydraul Res.* **50** (5), 451–464.

DEL ÁLAMO, J. C. & JIMÉNEZ, J. 2003 Spectra of the very large anisotropic scales in turbulent channels. *Phys. Fluids* **15**, 41–44.

BAKER, L., FRANKEL, A., MANI, A. & COLETTI, F. 2017 Coherent clusters of inertial particles in homogeneous turbulence. *J. Fluid Mech.* **833**, 364–398.

BALACHANDAR, S. & EATON, J. K. 2010 Turbulent dispersed multiphase flow. *Annu. Rev. Fluid. Mech.* **42**, 111–133.

BALAKUMAR, B. & ADRIAN, R. 2007 Large-and very-large-scale motions in channel and boundary-layer flows. *Phil. Trans. R. Soc. Lond.* A **365** (1852), 665–681.

BRANDT, L. 2014 The lift-up effect: the linear mechanism behind transition and turbulence in shear flows. *Eur. J. Mech. (B/Fluids)* **47**, 80–96.

CAMERON, S., NIKORA, V. & STEWART, M. 2017 Very-large-scale motions in rough-bed open-channel flow. *J. Fluid Mech.* **814**, 416–429.

CAPECELATRO, J. & DESJARDINS, O. 2013 An Euler–Lagrange strategy for simulating particle-laden flows. *J. Comput. Phys.* **238**, 1–31.

CAPECELATRO, J., DESJARDINS, O. & FOX, R. O. 2018 On the transition between turbulence regimes in particle-laden channel flows. *J. Fluid Mech.* **845**, 499–519.

CARTER, D. W. & COLETTI, F. 2018 Small-scale structure and energy transfer in homogeneous turbulence. *J. Fluid Mech.* **854**, 505–543.

CROWE, C. T. 2000 On models for turbulence modulation in fluid–particle flows. *Intl J. Multiphase Flow* **26** (5), 719–727.

DRITSELIS, C. D. & VLACHOS, N. S. 2008 Numerical study of educed coherent structures in the near-wall region of a particle-laden channel flow. *Phys. Fluids* **20** (5), 055103.

ELGHOBASHI, S. & TRUESDELL, G. 1993 On the two-way interaction between homogeneous turbulence and dispersed solid particles. I. Turbulence modification. *Phys. Fluids* A **5** (7), 1790–1801.

GUALA, M., HOMMEMA, S. & ADRIAN, R. 2006 Large-scale and very-large-scale motions in turbulent pipe flow. *J. Fluid Mech.* **554**, 521–542.

GUALTIERI, P., PICANO, F., SARDINA, G. & CASCIOLA, C. M. 2013 Clustering and turbulence modulation in particle-laden shear flows. *J. Fluid Mech.* **715**, 134–162.

HAMILTON, J. M., KIM, J. & WALEFFE, F. 1995 Regeneration mechanisms of near-wall turbulence structures. *J. Fluid Mech.* **287**, 317–348.

HUTCHINS, N. & MARUSIC, I. 2007 Evidence of very long meandering features in the logarithmic region of turbulent boundary layers. *J. Fluid Mech.* **579**, 1–28.

HWANG, Y. & BENGANA, Y. 2016 Self-sustaining process of minimal attached eddies in turbulent channel flow. *J. Fluid Mech.* **795**, 708–738.

JIMÉNEZ, J. 2011 Cascades in wall-bounded turbulence. *Annu. Rev. Fluid. Mech.* **44** (1), 27.

JIMÉNEZ, J. 2018 Coherent structures in wall-bounded turbulence. *J. Fluid Mech.* **842**.

JIMÉNEZ, J. & PINELLI, A. 1999 The autonomous cycle of near-wall turbulence. *J. Fluid Mech.* **389**, 335–359.

KIM, K. C. & ADRIAN, R. J. 1999 Very large-scale motion in the outer layer. *Phys. Fluids* **11** (2), 417–422.

KLINKENBERG, J., SARDINA, G., DE LANGE, H. & BRANDT, L. 2013 Numerical study of laminar–turbulent transition in particle-laden channel flow. *Phys. Rev.* E **87** (4), 043011.

LEE, J. H. & SUNG, H. J. 2011 Very-large-scale motions in a turbulent boundary layer. *J. Fluid Mech.* **673**, 80–120.

LEE, M. & MOSER, R. D. 2019 Spectral analysis of the budget equation in turbulent channel flows at high Reynolds number. *J. Fluid Mech.* **860**, 886–938.

LOZANO-DURÁN, A. & JIMÉNEZ, J. 2014 Effect of the computational domain on direct simulations of turbulent channels up to $Re_\tau = 4200$. *Phys. Fluids* **26** (1), 011702.

MARCHIOLI, C. & SOLDATI, A. 2002 Mechanisms for particle transfer and segregation in a turbulent boundary layer. *J. Fluid Mech.* **468**, 283–315.

MARUSIC, I., MATHIS, R. & HUTCHINS, N. 2010 Predictive model for wall-bounded turbulent flow. *Science* **329** (5988), 193–196.

MARUSIC, I. & MONTY, J. P. 2019 Attached eddy model of wall turbulence. *Annu. Rev. Fluid. Mech.* **51**, 49–74.

MICHAEL, D. 1964 The stability of plane Poiseuille flow of a dusty gas. *J. Fluid Mech.* **18** (1), 19–32.

MONCHAUX, R., BOURGOIN, M. & CARTELLIER, A. 2010 Preferential concentration of heavy particles: a Voronoï analysis. *Phys. Fluids* **22** (10), 103304.

MONCHAUX, R., BOURGOIN, M. & CARTELLIER, A. 2012 Analyzing preferential concentration and clustering of inertial particles in turbulence. *Intl J. Multiphase Flow* **40**, 1–18.

NEZU, I. 2005 Open-channel flow turbulence and its research prospect in the 21st century. *J. Hydraul. Engng* **131** (4), 229–246.

NEZU, I. & NAKAGAWA, H. 1993 *Turbulence in open-channel flows*. *IAHR-Monograph*. CRC Press.

PAN, Y. & BANERJEE, S. 1995 A numerical study of free-surface turbulence in channel flow. *Phys. Fluids* **7** (7), 1649–1664.

PAN, Y. & BANERJEE, S. 1996 Numerical simulation of particle interactions with wall turbulence. *Phys. Fluids* **8** (10), 2733–2755.

PARK, H. J., O'KEEFE, K. & RICHTER, D. H. 2018 Rayleigh–Bénard turbulence modified by two-way coupled inertial, nonisothermal particles. *Phys. Rev. Fluids* **3** (3), 034307.

POELMA, C. & OOMS, G. 2006 Particle–turbulence interaction in a homogeneous, isotropic turbulent suspension. *Appl. Mech. Rev.* **59** (2), 78–90.

RAWAT, S., COSSU, C., HWANG, Y. & RINCON, F. 2015 On the self-sustained nature of large-scale motions in turbulent Couette flow. *J. Fluid Mech.* **782**, 515–540.

REEKS, M. 1983 The transport of discrete particles in inhomogeneous turbulence. *J. Aero. Sci.* **14** (6), 729–739.

RICHTER, D. H. 2015 Turbulence modification by inertial particles and its influence on the spectral energy budget in planar Couette flow. *Phys. Fluids* **27** (6), 063304.

RICHTER, D. H. & SULLIVAN, P. P. 2014 Modification of near-wall coherent structures by inertial particles. *Phys. Fluids* **26** (10), 103304.

SAFFMAN, P. 1962 On the stability of laminar flow of a dusty gas. *J. Fluid Mech.* **13** (1), 120–128.

SARDINA, G., SCHLATTER, P., BRANDT, L., PICANO, F. & CASCIOLA, C. M. 2012 Wall accumulation and spatial localization in particle-laden wall flows. *J. Fluid Mech.* **699**, 50–78.

SCHOPPA, W. & HUSSAIN, F. 2002 Coherent structure generation in near-wall turbulence. *J. Fluid Mech.* **453**, 57–108.

SMITS, A. J., MCKEON, B. J. & MARUSIC, I. 2011 High-Reynolds number wall turbulence. *Annu. Rev. Fluid. Mech.* **43** (1), 353–375.

SUMER, B. M. & OGUZ, B. 1978 Particle motions near the bottom in turbulent flow in an open channel. *J. Fluid Mech.* **86** (1), 109–127.

TANAKA, T. & EATON, J. K. 2008 Classification of turbulence modification by dispersed spheres using a novel dimensionless number. *Phys. Rev. Lett.* **101** (11), 114502.

TOH, S. & ITANO, T. 2005 Interaction between a large-scale structure and near-wall structures in channel flow. *J. Fluid Mech.* **524**, 249–262.

TOWNSEND, A. A. 1980 *The Structure of Turbulent Shear Flow*. Cambridge University Press.

WALEFFE, F. 1997 On a self-sustaining process in shear flows. *Phys. Fluids* **9** (4), 883–900.

WANG, G., ABBAS, M. & CLIMENT, E. 2018 Modulation of the regeneration cycle by neutrally buoyant finite-size particles. *J. Fluid Mech.* **852**, 257–282.

WANG, G. & RICHTER, D. 2019 Modulation of the turbulence regeneration cycle by inertial particles in planar Couette flow. *J. Fluid Mech.* **861**, 901–929.

YAMAMOTO, Y., KUNUGI, T. & SERIZAWA, A. 2001 Turbulence statistics and scalar transport in an open-channel flow. *J. Turbul.* **2** (10), 1–16.

ZHAO, L., ANDERSSON, H. I. & GILLISSEN, J. J. 2013 Interphasial energy transfer and particle dissipation in particle-laden wall turbulence. *J. Fluid Mech.* **715**, 32–59.